

Thermoelectric properties and scattering mechanisms in natural PbS

Esteban Zuñiga-Puelles ¹, Volodymyr Levytskyi ¹, Ayberk Özden ², Tanju Gürel ³, Nebahat Bulut ²,
Cameliu Himcinschi ², Cem Sevik,^{4,5} Jens Kortus,² and Roman Gumeniuk ^{1,*}

¹*Institut für experimentelle Physik, TU Bergakademie Freiberg, Leipziger Straße 23, 09596 Freiberg, Germany*

²*Institut für theoretische Physik, TU Bergakademie Freiberg, Leipziger Straße 23, 09596 Freiberg, Germany*

³*Department of Physics, Tekirdağ Namik Kemal University, Tekirdağ TR-59030, Turkey*

⁴*Department of Mechanical Engineering, Eskisehir Technical University, Eskisehir TR-26555, Turkey*

⁵*Department of Physics & NANOLab Center of Excellence, University of Antwerp, Groenenborgerlaan 171, B-2020 Antwerp, Belgium*



(Received 24 February 2023; revised 27 April 2023; accepted 11 May 2023; published 30 May 2023)

X-ray diffraction and energy dispersive x-ray spectroscopic analyses showed a natural galena (PbS) crystal from Freiberg in Saxony (Germany) to be a single phase specimen [rock salt (NaCl) structure type, space group $Fm\bar{3}m$, $a = 5.932(1)$ Å] with stoichiometric composition and an enhanced dislocation density ($\delta \approx 10^{11}$ cm⁻²). The latter parameter leads to an increase of the electrical resistivity in the high-temperature regime, as well as to the appearance of phonon resonance with a characteristic frequency $\omega_{PR} = 3.8(1)$ THz. Being in the same range (i.e., 3–5.5 THz) with the sulfur optical modes of highest group velocities, it results in a drastic reduction (by $\sim 75\%$) of thermal conductivity (κ) at lower temperatures (i.e., < 100 K), as well as in the appearance of a characteristic minimum in κ at $T \approx 30$ K. Furthermore, the studied galena is characterized by phonon-drag behavior and by temperature dependent switch of the charge carrier scattering mechanism regime (i.e., scattering on dislocations for $T < 100$ K, on acoustic phonons for $100 \text{ K} < T < 170$ K and on both acoustic and optical phonons for $170 \text{ K} < T < 300$ K). The combined theoretical calculation and optical spectroscopic study confirm this mineral to be a direct gap degenerate semiconductor. The possible origins of the second-order Raman spectrum are discussed.

DOI: [10.1103/PhysRevB.107.195203](https://doi.org/10.1103/PhysRevB.107.195203)

I. INTRODUCTION

A significant growth of the energy consumption in the past few decades together with its low transformation efficiency (i.e., total losses of $\approx 70\%$ in form of a heat [1]) gave a new impetus in studies of thermoelectric (TE) materials. Allowing conversion of thermal gradients into electricity, a technology, which became already irreplaceable in the space exploration and is believed to possess a potential for energy harvesting in our daily life [2–5]. However, there are still challenges related to the insufficient efficiency for practical applications of known TE materials. A measure of TE efficiency is defined by the dimensionless figure-of-merit $zT = S^2T/\rho(\kappa_{ph} + \kappa_{el})$, where S stands for Seebeck coefficient, ρ as the electrical resistivity, κ_{ph} and κ_{el} represents the phononic and electronic thermal conductivities, respectively [6,7]. Obviously, high zT can be observed for TE material being simultaneously good electrical and a bad thermal conductor, which is a physical contradiction. To overcome it, two main routes are normally considered: (i) the optimization of the electrical transport (given as power factor $PF = S^2/\rho$), by tuning the charge carrier concentration n and/or their mobility μ via electron/hole doping [8–15], and/or (ii) the reduction of thermal conductivity by alloying of the material and/or by creating grain boundaries, point defects, bonding inhomogeneity, “rattling”

or anharmonic effects, etc., which should result in additional phonon scattering mechanisms [2,16–23].

Among the different factors, which could significantly reduce the thermal conductivity of a material and which has rarely been considered with respect to a possible improvement of the TE efficiency [24] is the so-called phonon resonance (PR). It has been reported for some mixed halides (e.g., $K_{1-x}Li_xBr$ and $K_{1-x}Li_xCl$) [25], $Na_{1-x}M_xCl_{1-y}Ha_y$ ($M = Li^+, K^+, Rb^+, Ag^+, Tl^+$, $Ha = F^-, Br^-, I^-$) [26], $Rb_{1-x}CN_xCl$ [27]) crystallizing with rock-salt structural arrangement [NaCl type, space group (SG) $Fm\bar{3}m$]. In these materials, a resonant interaction occurs between phonons and nonparamagnetic lattice point defects (induced by the dopants) and is characterized by a resonant frequency ω_{PR} , at which a minimum in κ_{ph} is observed [25,28]. Another scenario when PR behavior become possible is if the phonons are scattered by the vibrations of a filler-cation incorporated inside an enlarged anionic void (i.e., by the “rattling” effect). This is reported for some intermetallic Ge-containing clathrates [24]. Indeed, besides the materials crystallizing with NaCl structure type and filled Ge-clathrates PR was recently reported only for the doped hexagonal AlN [29] and monoclinic Cu₂Se (SG $C2/c$) [30]. Interestingly, the PR behavior in the latter was detected by inelastic neutron scattering and is not manifesting itself by a clear minimum in κ_{ph} .

Galena (PbS) is a naturally occurring and widespread narrow gap (theoretically calculated values are $E_g^{DFT} \sim 0.2\text{--}0.5$ eV [31–38], those from electronic absorption spectra:

*gumeniuk@physik.tu-freiberg.de

$E_g^{\text{abs}} \sim 0.37\text{--}0.40$ eV [39,40] and from optical absorption measurements $E_g^{\text{opt}} \sim 0.40\text{--}0.44$ eV [33,41] semiconducting diamagnetic sulfide, crystallizing with the rock-salt structure type [42–44]. Since this mineral can be found in form of large (i.e., > 1 cm³) and pure crystals, it was industrially used in the production of radio receivers in the beginning of the last century [45]. Moreover, the semiconducting properties of galena are easily tunable due to unlimited solubility of selenium and tellurium (i.e., $\text{PbS}_{1-x}\text{Se}_x$ and $\text{PbS}_{1-x}\text{Te}_x$) in it [46,47]. Among the numerous applications, these materials belong to the group of those with the most promising TE efficiency [6,48–51].

One more intriguing property of PbS is a metallic-like resistivity (i.e., ρ increases with T), which is mainly due to enhanced charge carrier concentration varying in the atypical for a semiconductor range of $10^{16\text{--}19}$ cm⁻³ and good mobility [$\mu \sim 10^{1\text{--}3}$ cm²(V s)⁻¹] [36,39,40,52–57]. In combination with relatively high Seebeck coefficients ($|S| \sim 100\text{--}300$ $\mu\text{V K}^{-1}$) [34,39,52,55] and moderate thermal conductivity ($\kappa \sim 2\text{--}5$ W m⁻¹ K⁻¹ [36,39,52,55]) one obtains $zT \sim 0.2\text{--}0.4$ at 600 K. Interestingly, the number of reports devoted to the low temperature properties of galena is rather small [54,56–58].

In this paper, we have investigated a natural PbS crystal originating from Freiberg (Germany) by structural, spectroscopical, magnetic, and thermodynamic methods. It has been found to be of outstanding chemical purity and to be characterized by enhanced dislocation density. The latter is obviously a reason for unusually high charge carrier concentration, as well as phonon resonant behavior, which is rare for semiconductor. The natural galena from Freiberg is found to reveal a phonon-drag behavior in the low-temperature regime and to show three different mechanisms of charge carrier scattering on phonons, which become activated with increasing temperature.

II. EXPERIMENTAL

Natural PbS single crystal with the dimensions $2 \times 1.6 \times 1.2$ cm³ originates from Freiberg in Saxony (Germany). In this region galena occurs in four different hydrothermal stages [42,59]; however, the accurate identification of the formation stage of our specimen is complicated due to its high purity (see discussion below).

The sample was characterized by powder- (PXRD) and single crystal x-ray diffraction (SCXRD). The PXRD patterns were collected on an image plate Guinier camera Huber G670 (Cu- $K\alpha_1$ radiation, $\lambda = 1.540562$ Å, $5^\circ \leq 2\Theta \leq 100^\circ$, $\Delta\Theta = 0.005^\circ$). The SCXRD data were collected on a Bruker AXS D8 Quest diffractometer, equipped with a Photon100 area detector and Mo- $K\alpha$ radiation ($\lambda = 0.71073$ Å). The analysis of the data and image integration were performed with the CrysAlisPro software [60]. Both PXRD and SCXRD crystal structure refinements were performed using the WinCSD program package [61].

A representative area of the sample was embedded in a conductive resin, grinded and polished. The final polishing was performed with 0.25 μm diamond powder. The obtained surfaces were analysed by scanning electron microscopy (SEM) and spectroscopic ellipsometry. Local chemical composition

and microstructure analyses were carried out using a SEM-JEOL JSM 7800F microscope equipped with Bruker Quantax 400, XFlash 6||30 (silicon drift detector) energy dispersive x-ray (EDX) spectrometer.

Spectroscopic ellipsometry was performed on polished samples at 50° , 55° , 60° , and 65° incidence angles, in the 0.73–6 eV range using an M2000 J.A. Woollam ellipsometer. Fourier transform infrared (FTIR) absorption measurements were performed in the midinfrared spectral range on a Bruker Tensor 27 spectrometer, in the energy range 0.12–0.40 eV.

Nonpolarized Raman spectra were collected in a Horiba LABRAM System-HR-800 (CCD camera, 600 grooves per mm grating, with a HeNe laser 633 nm and an 50X objective N.A., of 0.5). The initial spectrometer calibration was performed by use of the 520.6 cm⁻¹ peak from a Si[111] standard. Neon calibration-lamp spectra were recorded after each measurement to correct any shift during the Raman measurements. Temperature-dependent Raman spectra were obtained with a Linkam THMS-600 cooling-heating stage, continuously cooled by liquid nitrogen vapor-flow between 100–300 K. To prevent any drift of the sample and enhance the thermal contact, it was fixed to the stage with silver paste. All presented results correspond to the average of 10 different measured points.

Optothermal Raman (OTR) technique with a thermal model for single crystals and/or bulk materials was utilized to get Raman thermal conductivity between 100–300 K. For more details on this experiment we refer to the Supplemental Materials (SM) [62] and our recent papers [63,64].

Low temperature (LT, $T \leq 300$ K) magnetic susceptibility [$\chi(T)$], specific heat capacity [$c_p(T)$], charge carrier concentration [$n(T)$], and mobility [$\mu(T)$], as well as electrical resistivity [$\rho(T)$], Seebeck coefficient [$S(T)$], and total thermal conductivity [$\kappa(T)$] were measured with VSM, HC, VdP-Hall, and TTO modules of DynaCool-12 from Quantum Design. High temperature (HT, $300 \text{ K} \leq T \leq 600 \text{ K}$) $\rho(T)$ and $S(T)$ were obtained on a ULVAC ZEM-3 device.

The electronic structure for galena within the generalized gradient approximation (GGA) of the density functional theory (DFT) was calculated using the full-potential FPLO code (version 18.00-52) [65]. The calculation was performed applying the scalar relativistic approximation using the exchange-correlation potential by Perdew and Wang [66]. The k mesh included $20 \times 20 \times 20$ points in the first Brillouin zone.

For the first principles simulation of PbS Seebeck coefficients, its crystal structure was optimized using Quantum Espresso [67]. Then, its electronic transport properties were calculated applying the BoltzTrap code [68]. The generalized gradient approximation (GGA) with PBE parametrization [69] has been used for the exchange-correlation functional [70]. The interactions between the ions and electrons were described by the projector augmented wave method (PAW) together with a plane wave cut-off of 90 Ry and a converged k -grid with $20 \times 20 \times 20$ k points. The energy cut-off was chosen according to convergence tests and its criteria was set up to 10^{-8} .

For the determination of phonon dispersion relations (PDR) and phonon density of states (PDOS), DFT calculations were performed within Vienna *Ab initio* Simulation

Package (VASP) [71]. The exchange and correlation functionals, based on the generalized gradient approximation (GGA), were parameterized using Perdew-Burke-Ernzerhof (PBE) scheme [69]. Projector augmented wave (PAW) pseudopotentials [72] were used to represent the interaction between ions and electrons. For the energy cut-off of plane waves, we have used a converged 400 eV value together with a convergence criterion of 10^{-7} eV in the self-consistent-field calculations. The geometric optimization process is performed with k grid of $8 \times 8 \times 8$. In the calculations of PDR and PDOS, the second-order interatomic force constants (IFCs) are obtained from supercell finite-difference method as implemented in PHONOPY code [73]. We have used a $4 \times 4 \times 4$ supercell and a $2 \times 2 \times 2$ k grid in order to obtain second-order IFCs. Additionally, in order to account for the long range dipole interactions in the dynamical matrix, the required parameters of Born effective charges and dielectric constants were obtained from density functional perturbation theory (DFPT) [74] with a denser $21 \times 21 \times 21$ k grid. The third-order force constants were also obtained with finite-difference method with $4 \times 4 \times 4$ supercell and a $2 \times 2 \times 2$ k grid by using the thirdorder.py script [75]. By considering the interactions to fourth-nearest neighbors, we used 156 different supercell configurations with a 0.01 Å displacement of atomic perturbations. After obtaining the third-order IFCs, the phonon transport properties are calculated by solving the phonon Boltzmann transport equation (pBTE) as implemented in the ShengBTE code [75]. We considered the phonon-phonon interactions as well as the isotopic scattering and boundary scattering mechanisms [76]. The q grid in the ShengBTE calculations was $32 \times 32 \times 32$ and the scalebroad factor was tested for 0.1 and 1.0. Since the difference between two factors found to be less than 2.5%, subsequent calculations have been performed with 0.1.

III. RESULTS

A. Crystal structure and sample characterization

Single crystal x-ray diffraction (SCXRD) was performed on a mechanically extracted piece from the crashed specimen. The obtained dataset were indexed with a unit-cell parameter given in Table I. The analysis of the extinction conditions indicated a face-centred lattice without additional extinctions [i.e., five possible space groups (SG): $F23$, $Fm\bar{3}$, $F432$, $F43m$, and $Fm\bar{3}m$]. This prompted us to choose the known for PbS structural model of rock salt (SG $Fm\bar{3}m$) [44,54,77] as a starting one for the further refinement. It converged with the parameters listed in Table I. During the refinement special attention was paid to the correlation between atomic displacement (B_{iso}) and occupational parameters (G). The attempts to decrease the occupancies by artificially reduced B_{iso} always resulted in the increased reliability factors, which brought us to the conclusion that the studied mineral is of stoichiometric composition. This finding is in good agreement with the performed electron dispersive x-ray spectroscopy (EDX) analysis (Table I). The obtained structural model was also successfully applied for the refinement of the powder XRD (PXRD) data (Fig. 1, $R_I = 0.022$, $R_P = 0.063$). No additional peaks were observed in the refined PXRD

TABLE I. Crystallographic data for PbS, [$Z=4$; Pb in $4a$ (0, 0, 0); S in $4b$ ($1/2, 1/2, 1/2$)].

Refined composition	PbS
EDXS composition	Pb _{1.1(1)} S _{0.9(2)}
Space group (SG)	$Fm\bar{3}m$ (N ^o 225)
From PXRD a (Å)	5.932(1)
Radiation, λ (Å)	Mo-K α , 0.71073
Calculated density d (g cm ⁻³)	7.51(2)
Scan; step (°); $N(\text{images})$	ϕ and Ω ; 1; 1498
Maximal 2Θ (°)	65.82
Ranges in h, k, l	$-8 \leq h \leq 7$ $-9 \leq k \leq 8$ $-9 \leq l \leq 9$
Absorption correction	Numerical
$T(\text{max})/T(\text{min})$	1.00/0.55
Absorption coeff. (mm ⁻¹)	79
$N(\text{hkl})$ measured	935
$N(\text{hkl})$ unique	37
R_{int}	0.023
Observation criterion	$F(\text{hkl}) \leq 4\sigma(F)$
Refined parameters	5
$R_F; R_W$	0.020; 0.022
Residual peaks ($e \text{ \AA}^{-3}$)	-0.22/0.28
$d_{\text{Pb-S}}$ (Å)	2.980(1)
$B_{\text{iso}}(\text{Pb})^a$ (Å ²)	1.574(4)
$B_{\text{iso}}(\text{S})^a$ (Å ²)	1.47(1)

$$^a B_{\text{iso}} = B_{11} = B_{22} = B_{33}; B_{12} = B_{13} = B_{23} = 0.$$

pattern, which confirms again the purity of the studied here mineral.

As it is known the structural arrangement of rock salt can be obtained by the centring of the edges (by S atoms in case of the PbS structure) of simple fcc structure (the sublattice is formed by Pb atoms in PbS) (inset to Fig. 1). As expected, the interatomic distances in the refined here PbS structure (Table I) are in good agreement with the sums of the corresponding ionic radii (i.e., $d_{\text{Pb}^{2+}\text{-S}^{2-}} = 3.03 \text{ \AA}$) [78].

The crystallite size (D in Å) is related to the full-width at half-maximum (β in rad) of PXRD reflections by the

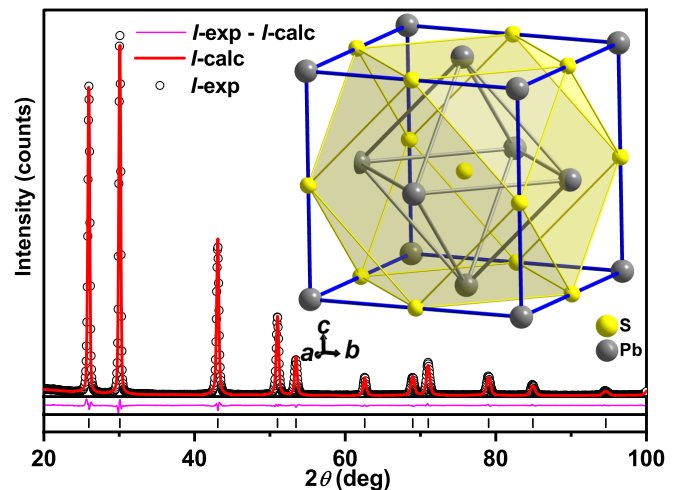


FIG. 1. PXRD pattern and Rietveld refinement for natural PbS, as well as structural arrangement of Pb and S atoms in galena.

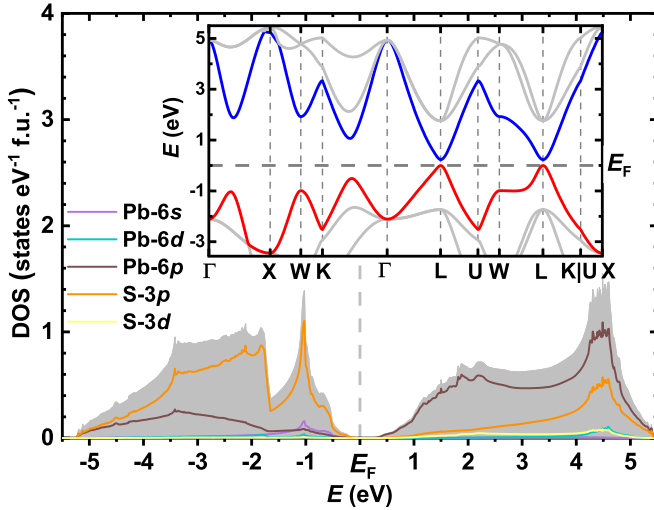


FIG. 2. Total and atomic resolved electronic density of states for PbS. Inset: The band structure of galena with highlighted valence (VB) and conduction (CB) bands, red, and blue lines respectively.

following equation [79]:

$$\beta \cos \theta = \frac{k\lambda}{D} + 4\epsilon \sin \theta \quad (1)$$

where $k = 1$ is a crystallite shape constant, λ corresponds to the x-ray radiation wavelength and θ denotes the Bragg angle. Hence, the strain component $\epsilon = 2.5(1) \times 10^{-3}$ is estimated from the slope of Williamson-Hall plot (i.e., $\beta \cos \theta$ vs $\sin \theta$ dependence, Fig. S1 in SM [62]) whereas its linear extrapolation to $\theta = 0$ is the crystallite size $D = k\lambda/\beta \cos \theta = 214(52)$ Å. Further, the dislocation density $\delta = D^{-2} = 2.3(5) \times 10^{11} \text{ cm}^{-2}$ is calculated [80,81].

B. Electronic and phononic structures

The electronic density of states (DOS) calculated from the structural data presented in Table I are shown in Fig. 2. The valence band (VB) for PbS is consisting of three separate regions: (i) a narrow low-energy band extending from -13.6 eV to -11.8 eV dominated by S-2*p* states (not shown in Fig. 2); (ii) a band (-8.9 eV to -6.1 eV) due to mixing of Pb-6*s*, S-3*s*, and S-3*p*, and (iii) a broad high-energy band extending from -5.24 eV to the Fermi level E_F consisting of S-3*p* and Pb-6*p* electrons. In the electronic structure of PbS, the VB is separated from the conduction band (CB) by an energy gap $E_g^{\text{DFT}} = 0.23$ eV. This value is in agreement with the earlier reports [33,35–37]. In the energy range 0.23–5.45 eV, there are empty Pb-6*p* and S-3*p* states.

The closest to the Fermi level (E_F) bands in both VB and CB are nearly parabolic (inset of Fig. 2). Since the conduction band minimum (CBM) and the valence band maximum (VBM) at L point are in front of each other, PbS is obviously a direct semiconductor.

The sharpness of CBM and VBM indicates them to be light bands and assumes rather small effective masses (m^*) of the charge carriers. And indeed, the calculated from $m^* = \hbar(d^2E/dk^2)^{-1}$ values for m_h^* (holes) and m_e^* (electrons) are $\leq |0.2|$ (Table II). Also, the effective masses [$m^* \approx 0.11(3)$]

TABLE II. Effective holes (m_h^*) and electrons (m_e^*) masses normalized to electron rest mass ($m_e = 9.11 \times 10^{-31}$ kg) for VBM and CBM from the band structure calculations.

	VBM (m_h^*/m_e)	CBM (m_e^*/m_e)
Γ -X	0.11	0.09
W	0.11	0.11
K- Γ	0.17	0.14
L	0.11, 0.11	0.12, 0.14

reveal nearly isotropic behavior with the only exception for the VBM at K- Γ for which a small deviation from the average is observed.

The calculated phonon band structure in comparison with experimental data obtained in [82] from inelastic neutron scattering (INS) at RT are shown in inset of Fig. 3. As one can see, there is an excellent agreement between the theory and experiment for the acoustic modes, whereas the longitudinal optical (LO) modes become slightly lowered throughout the Brillouin zone. The calculated at 0 K transversal optical (TO) modes are largely underestimated at Γ point compared with experimental data. This underestimation is acceptable since lead chalcogenides [83–85] are well known to reveal an increase of TO modes frequencies with increasing temperature. Also, the second-order Raman spectra studies for PbS show similar increment of frequencies with increasing temperature [86,87]. One important feature of the phonon dispersion is the gap between acoustic and optical modes. This gap, together with a dip behavior of TO phonons close to Γ point, presents a dispersion nesting behavior between longitudinal acoustic (LA) and TO modes [85].

The total and atom-projected phonon density of states (PDOS) are presented in Fig. 3. The low-frequency acoustic modes in PbS are completely constituted by the vibrations of the heavy lead atoms whereas light sulfur atoms compose

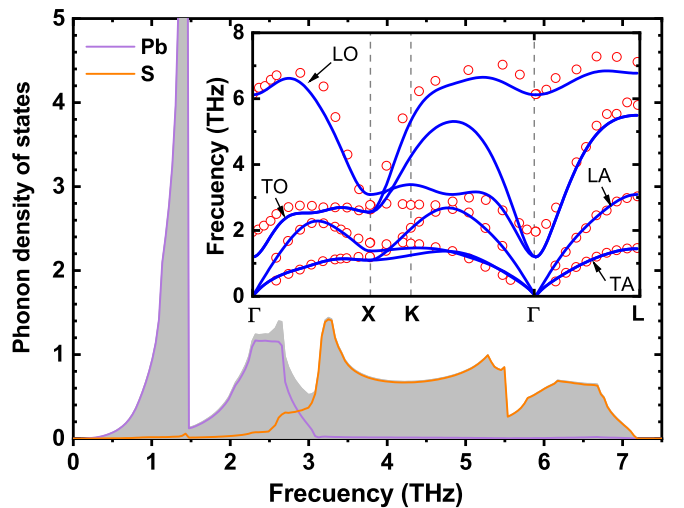


FIG. 3. Total and atom-projected phonon density of states of PbS. (Inset) Calculated phonon dispersion relations (PDR) with labeled longitudinal and transversal acoustic (LA and TA) and optical (LO and TO) modes of PbS in comparison with inelastic neutron scattering data (red circles) from [82].

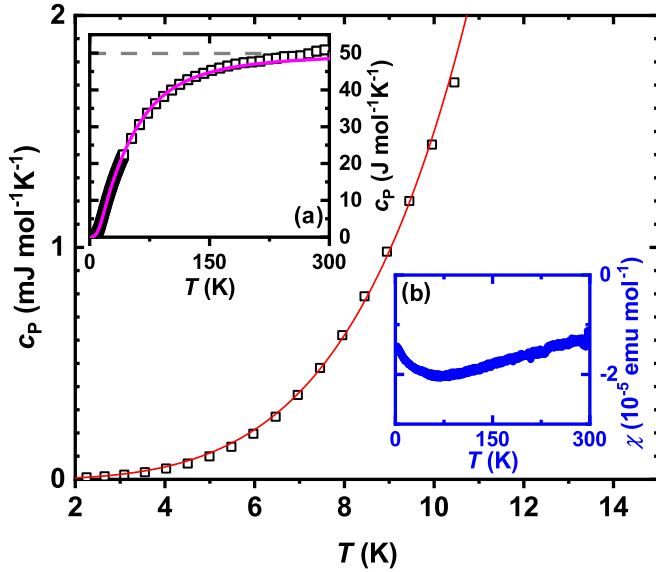


FIG. 4. Low-temperature specific heat capacity $c_p(T)$ together with the fit (red line) to Eq. (2) for 2–10 K. Inset a: Temperature dependence of the specific heat capacity [$c_p(T)$] including the two-term Debye model fit (magenta line) and Dulong-Petit limit (gray dashed line). Inset b: Temperature dependence of the corrected magnetic susceptibility [$\chi(T)$].

the optical modes of higher frequencies. The flat band of low TO branch in the $X - K - \Gamma$ direction indicate the large amount of localized states in the 3–3.5 THz range forming a peak. All observed in the performed calculations features are resembling those reported for PbS in [37,88,89].

C. Magnetic susceptibility and heat capacity

The temperature dependence of the corrected by the diamagnetic increments [90] magnetic susceptibility [$\chi(T)$] of PbS is shown in inset b of Fig. 4. It is negative and nearly temperature independent, which indicate galena to be a diamagnet. The weak curvature in $\chi(T)$ (i.e., decrease from 2 to ≈ 70 K with further increase up to 300 K, both changes are negligibly small, i.e., by $\approx -5 \times 10^{-7}$ emu mol $^{-1}$) is atypical for diamagnetism. Such an effect can be related to either a steep slope of the DOS near the Fermi level in a metallic system [91] or to the dependence of χ from the charge carrier concentration. The latter scenario is reported in n -doped GaAs, where a weak curvature in $\chi(T)$ is also a case [92]. Since PbS is not a metal and it reveals no temperature dependence of charge carrier concentration [$n(T)$] (cf. inset of Fig. 8) obviously neither of the proposed scenarios is explaining its $\chi(T)$. The only explanation would be the contributions of some micro impurities, which agrees well with the high sensitivity (i.e., ppm range) of the used magnetometer.

The specific heat of PbS in the temperature range 2–10 K can be described (red line in Fig. 4) by *ansatz*,

$$c_p(T) = \gamma T + \beta T^3 + \delta T^5 \quad (2)$$

with the Sommerfeld coefficient of the electronic specific heat $\gamma = 2.0(1.5) \times 10^{-4}$ J mol $^{-1}$ K $^{-2}$ and phononic contributions $\beta = 7.02(9) \times 10^{-4}$ J mol $^{-1}$ K $^{-4}$ [correspond-

TABLE III. Parameters from heat capacity fit to Eq. (3) in comparison to reported values.

	This paper	Fit [88]	NXRD [88]	PXRD [77,88]
Θ_{D1} K	109(1)	110(3)	120.2(6)	116
Θ_{D2} K	306(3)	326(5)	324(2)	317

ing to the Debye temperature $\theta_D = 173(1)$ K] and $\delta = 7.96(8) \times 10^{-6}$ J mol $^{-1}$ K $^{-6}$. A very small γ corresponding to a finite density of states at the Fermi level is observed for PbS in line with the temperature independent charge carrier concentration (cf. Fig. 8) as well as previous reports for such similar semiconductors as, e.g., FeS $_2$ [93,94], PbCuSbS $_3$ [63], etc.

Considering the phononic spectra for galena, authors of [88] derived two Debye terms from cut-off frequencies obtained from integration of the calculated partial PDOS for the Pb $^{2+}$ and S $^{2-}$ ions and thus applied the following model [Eq. (3)] to describe $c_p(T)$ in the whole temperature range:

$$c_p(T) = \gamma T + \sum_{i=1}^2 C_{Di}(T) \quad (3)$$

with

$$C_{Di}(T) = 3N_{Di}R \left(\frac{T}{\Theta_{Di}} \right)^3 \int_0^{\Theta_{Di}/T} \frac{x^4 e^x}{(e^x - 1)^2} dx \quad (4)$$

where γ is fixed to the value above, $N_{Di} = 6$ is a total number of phononic modes for PbS, R gas constant, Θ_{Di} Debye temperature, and x an integration variable. A fit to such a model excellently works in the temperature range 2–250 K (inset a to Fig. 4). The obtained parameters are collected in Table III. They agree well with those previously reported from $c_p(T)$ measurements as well as from neutron- and x-ray diffraction experiments. On the other hand, the two-term model fails in the description of $c_p(T)$ of PbS for $T > 250$ K despite the Dulong-Petit limit ($3nR = 49.86$ J mol $^{-1}$ K $^{-1}$) is already reached at 274(1) K (grey dashed line in inset a of Fig. 4). This discrepancy is related to the estimation of the sample surface area and infrared emissivity contribution to $c_p(T)$ measurements, as discussed in [95]. No features (i.e., no maximum in the c_p/T^3 vs T presentation) indicating any “rattling” effect are observed.

D. Spectroscopic ellipsometry and Raman spectroscopy

The obtained PbS ellipsometric spectra has been fitted by a two-phase model bulk galena/ambient. The performed fit confirmed the Kramer-Kronig consistency of the optical constants. Then, the real (ϵ_1) and imaginary (ϵ_2) parts of the dielectric function were calculated. The obtained ϵ_1 and ϵ_2 are in good agreement with the earlier published data in [96] (inset to Fig. 5).

The absorption coefficient (α) has been obtained from dielectric function and IR absorption measurements. The further analysis of the plot of $(\alpha E)^{1/2}$ vs photon-energy reveals a single slope (Fig. 5) indicating PbS to be a direct band-gap semiconductor in agreement with performed theoretical calculations. The optical band gap $E_g^{\text{opt}} = 0.38(1)$ eV was estimated by linear extrapolation of $(\alpha E)^{1/2}$ to zero absorption.

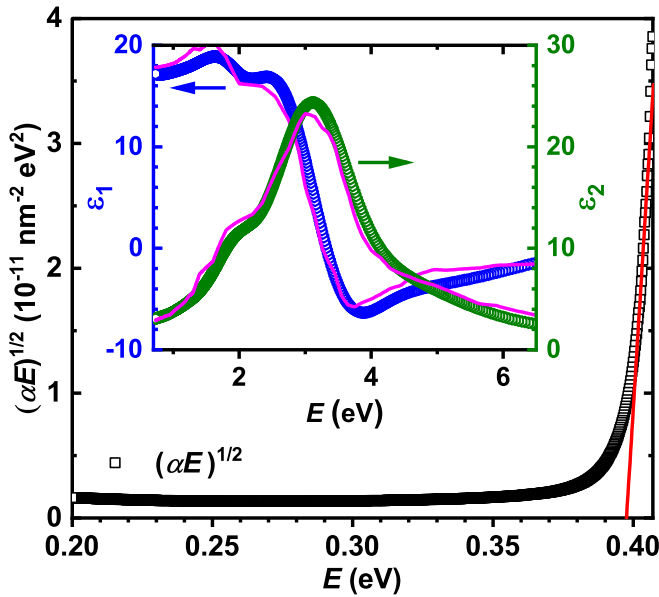


FIG. 5. Experimental absorption coefficient (α) in IR range of PbS against the photon energy (E), the red line represents the linear projection to zero absorption. Inset: Experimentally estimated real (ϵ_1) and imaginary (ϵ_2) parts of dielectric function from ellipsometric spectroscopy in comparison with data from [96] (magenta lines).

And again, this value fairly agrees with the calculated one $E_g^{\text{DFT}} = 0.23$ eV. A narrow band gap in the studied sample is additionally evidenced by the fact that ϵ_2 is still showing absorption at the lowest measured energy (~ 0.7 eV) (inset of Fig. 5).

The obtained E_g^{opt} is in good agreement with the values from the analogous optical measurements [33,41,97], from electronic absorption spectra [39,40] as well as theoretically calculated ones [38].

In accordance with the group theory analysis, the first-order Raman modes are forbidden for compounds crystallizing with the rock-salt structure type. However, second-order spectrum can be in general observed for such structures [98,99], which is the case for PbS [86,100], PbSe, PbTe, $\text{Pb}_{1-x}\text{Sn}_x\text{Se}$ [101] etc. The appearance of Raman active modes in galena has been attributed to the combined scattering effects of longitudinal (LA) and/or transversal (TA) acoustic and optical (LO and TO) phonons.

The Raman spectra measured at different points of the studied sample were identical, confirming its homogeneity, stoichiometric composition, no impurities and high crystallinity. A typical spectrum measured at 100 K and normalized to the highest intensity, together with peak descriptions, is presented in Fig. 6. In agreement with the previous reports for synthetic and natural samples [86,87,100], we observe five different bands between 150–500 cm^{-1} indicated further as P1, P2, P3, P4, and P5 (Fig. 6). The peak positions and their second-order origins proposed in the literature [100] are collected in Table IV.

The Raman spectra for PbS measured at different temperatures are shown in inset to Fig. 6. They reveal a clear shift of all observed bands with the exception of P2 (Fig. S2 in SM [62]). To characterize the observed shifts the tem-

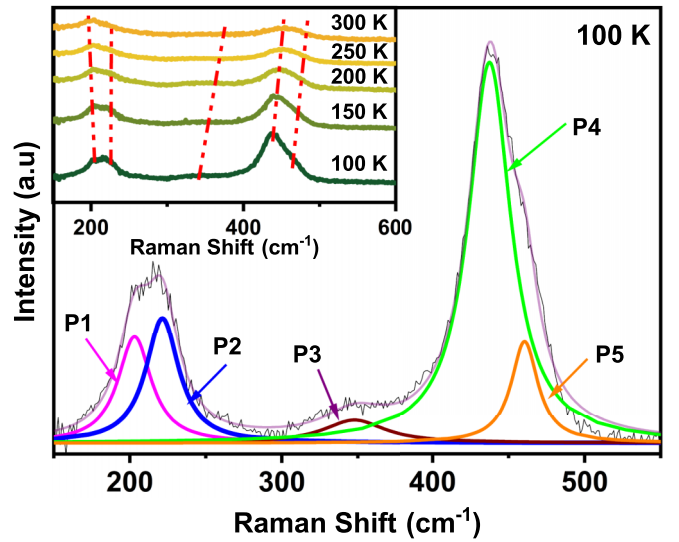


FIG. 6. Raman spectra recorded at 100 K for PbS including peak description and labels. Inset: Temperature dependent evolution of the Raman spectra for PbS, red dashed lines represents the shift of corresponding peak centres.

perature dependencies of the peaks positions were fit to $\omega(T) = \omega_0 + \omega_1 T$. The obtained fit-parameters are collected in Table IV.

The temperature evolution of the P1 band reveals a negative slope, which indicates phonon softening arising due to thermal expansion and phonon anharmonicity as described by Balkanski-Klemens model [102]. This observation suggests P1 band to originate either from LO modes near the Γ point (cf. Fig. 3) [86] or from the appropriate excitations allowed by the well-known Fröhlich resonance mechanism [103]. The former scenario is rather impossible, since the first-order Raman spectra are forbidden in the case of PbS as discussed above, whereas the latter one seems to be the most reliable.

On the other hand, P2, P3, P4, and P5 bands reveal anomalous positive slopes (Table IV and Fig. S2 in SM [62]), that can be referred to the phonon hardening, which may again occur in compounds revealing first-order Raman spectra. Also, this rare case is only observed for PdO [104] and VO_2 [105]. Such a behavior in PbS can be attributed to two-phonon scattering nature of these bands [86,87]. However, the understanding of two phonon scatterings processes is hampered

TABLE IV. Raman peak positions (ω_{100}) in the spectrum measured at 100 K together with the parameters obtained from the linear fits of the temperature dependencies of peak positions to $\omega(T) = \omega_0 + \omega_1 T$ as well as reported origins of the corresponding Raman bands appearing due to scattering of different phonons (e.g., LA, LO, TO) [100]. All values are given in cm^{-1} .

Mode	ω_{100}	ω_0	ω_1	Peak origin
P1	204(2)	207.4(5)	-0.023(2)	LO or 2TO
P2	223(2)	223(1)	0.003(6)	LO or 2TO
P3	345(4)	333(3)	0.11(1)	LA + LO
P4	438(1)	435(1)	0.034(5)	2 LO
P5	461(1)	457.1(7)	0.033(2)	2 LO

by the absence of a theoretical model that would describe the temperature dependence of the second-order Raman modes.

Using the optothermal Raman (OTR) technique, as described and discussed in SM [62] and in our previous papers [63,64], we calculated the phononic part of thermal conductivity, which agree well with those from the direct measurement (see Fig. 9 below). However, further proceeding aiming separation of the scattering of optical phonons, which are Raman active, into three-phonon and four-phonon decay mechanisms, as it was successfully performed for bourbonite applying Klemens-Balkanski model [63] was impossible. This is again because of the second-order origin of Raman active modes in PbS.

E. Electrical transport

In agreement with the previous reports [33,36,40,52,53,55,106], we observe low (as for a semiconductor) and increasing with temperature electrical resistivity [$\rho(T)$] for PbS [Fig. 7(a)]. Such a behavior together with large Seebeck coefficient [$S(T)$] [see Fig. 7(b)] and temperature independent charge carrier concentration (inset to Fig. 8) indicates galena to be a degenerate semiconductor. However, as one can see from Fig. 7(a), the specimen studied here reveals a factor of ~ 2 –4 larger resistivity above RT compared with synthetic analogues. This is most probably due to some minor impurities [i.e., reducing $\rho(T)$] in the latter samples. However, to clarify this point a chemical and spectroscopic analyses after sintering of synthetic specimens should be performed.

The temperature dependencies of Seebeck coefficients of the here investigated natural PbS together with those of some synthetic samples are depicted in Fig. 7(b). All of them are negative, indicating electrons to be the dominating charge carriers. The only exception [showing positive $S(T)$ and thus a p -type conductivity] is the specimen synthesized by the hydrothermal method and most probably contaminated with components of the used dissolving agent (e.g., NaOH) [52]. The natural specimen reveals the largest absolute values of $S(T)$, which indicates a lower charge carrier concentration in agreement with the observed $\rho(T)$ trends (i.e., tentatively $\rho^{-1} \propto n$ and $S \propto n^{-1}$) [107]. Also, the minima in $S(T)$ for synthetic samples are obviously shifted towards higher temperatures. To understand such an effect we calculate the energy gap for the mineral using the Goldsmid-Sharp formula [108] $E_g^S = 2e|S_{\max}|T_{\max} = 0.51$ eV. This value is somewhat larger than the optical one (i.e., $E_g^S/E_g^{\text{opt}} \approx 1.13$), which indicates either a breakdown of Maxwell-Boltzmann statistics (used to derive the Goldsmid-Sharp formula) or that this material has a very large/small majority-to-minority carrier weighted mobility (μ) ratio (A) given as [109]

$$A = \frac{\mu_{\text{maj}}}{\mu_{\text{min}}} \left(\frac{m_{\text{maj}}^*}{m_{\text{min}}^*} \right)^{3/2}. \quad (5)$$

Using the approach proposed in Fig. 4 of [109], we found $A = 3$ to 5 for our sample. It confirms that the shifted minima in $S(T)$ towards higher temperatures are due to smaller A -values. In accordance with Eq. (5) such a scenario is possible if μ_{maj} would become smaller (i.e., appearance of additional

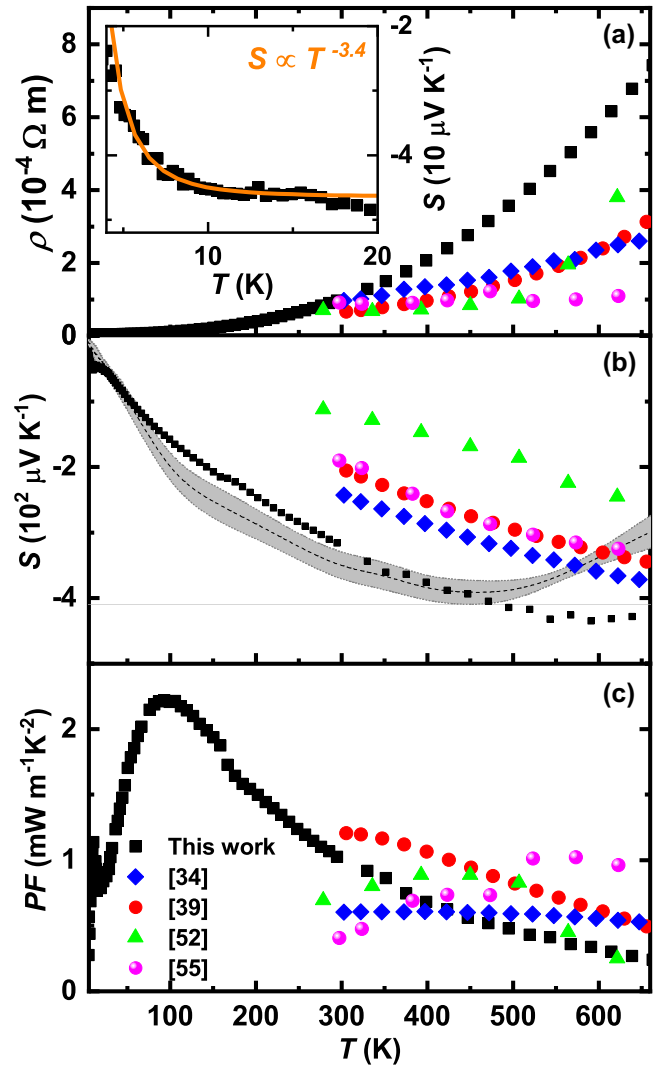


FIG. 7. Temperature dependencies of the electrical resistivity (a), of the experimentally obtained (data from [52] were multiplied by -1 for better visualization) and theoretically calculated [assuming charge carrier concentration $1.5(3) \times 10^{18} \text{ cm}^{-3}$] (gray area) Seebeck coefficient (b) and of power factor (c) for natural PbS in comparison with earlier reported nondoped synthetic samples. Inset to (a): $S(T)$ for 4–20 K, orange line shows the fit $\propto T^{-3.4(1)}$ corresponding to phonon-drag behavior.

scattering centers in the sample) or if μ_{min} would increase (possible in the case of some small off-stoichiometry of the specimens).

The absolute values of Seebeck coefficient for natural PbS smoothly decreases with decreasing temperature down to ~ 170 K. The kink at $T_k = 166$ K is due to the change of the scattering mechanism, as evidenced by the temperature dependence of charge carrier mobility (see analysis below). Further, $S(T)$ decreases almost linearly down to ~ 20 K and below this temperature it is following $S(T) \propto T^n$ dependence [see fit in inset to Fig. 7(a)]. Since, such a behavior occurs at $T \leq \Theta_D/5 \approx 35$ K and $n = -3.4(1) \approx -7/2$ obtained from the fit, a phonon drag conduction mechanism takes place in single crystalline PbS. As it is known, for the realization of this scenario theory predicts $n = -7/2$ in the absence of

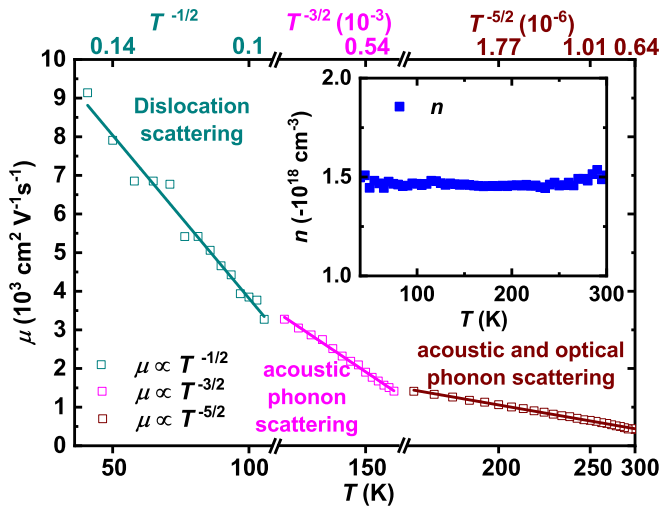


FIG. 8. Temperature dependence of charge carrier mobility for natural PbS on the temperature (lower scale) and on T^a with $a = -1/2, -3/2$ and $-5/2$ (upper scale) corresponding to the scattering by dislocations, acoustic as well as combined acoustic and optical phonons, respectively. Inset: Temperature dependence of charge carrier concentration.

grain boundary scattering [110]. This would also explain the absence of the effect in the synthetic bulk polycrystalline samples [54] [Fig. 7(b)].

The theoretically calculated (using BoltzTrap code) $S(T)$ is nicely reproducing our experimentally obtained dependence in the temperature range ~ 30 – 500 K [Fig. 7(b)]. However, the theory does not simulate the phonon drag effect below ~ 30 K. The deviation of theoretical values above ~ 500 K is due to the code assumption that the relaxation time is constant and that the bipolar conduction is not taken into account [68].

The temperature dependencies of the thermoelectric power factor [$PF(T)$] are depicted in Fig. 7(c). $PF(T)$ for natural PbS passes through a maximum at ~ 90 K and in the whole studied here temperature range its values are comparable with those of such state-of-the-art thermoelectric materials as, e.g., SnSe (undoped $PF_{\max} \sim 0.3$ mW m $^{-1}$ K $^{-2}$ at 300 K or doped $PF_{\max} \sim 1.13$ mW m $^{-1}$ K $^{-2}$ at ~ 575 K) [111], Cu $_2$ Se $_{1-x}$ S $_x$ ($PF_{\max} = 0.8$ mW m $^{-1}$ K $^{-2}$ at 800 K) [112] or doped Mg $_3$ Sb $_2$ ($PF_{\max} = 0.9$ – 2 mW m $^{-1}$ K $^{-2}$ at 700 K) [113,114]. Interestingly, values of $PF(T)$ are very close for all presented samples for $T \geq 300$ K, which is due to the fact that the larger $|S|(T)$ counterbalances the higher $\rho(T)$.

The temperature dependence of charge carrier concentration [$n(T)$] (Fig. 8) was deduced from the measured Hall coefficient (R_H) using relation $R_H = 1/en$. It is nearly temperature independent in the 50–300 K range with $n \approx 10^{18}$ cm $^{-3}$. This value is 6–8 orders of magnitude larger than those for classical semiconductors ($n \approx 10^{10-12}$) [107] and is nearly the same as for the materials revealing the nowadays highest known TE efficiency (e.g., SnSe [111], half-Heusler and some Zintl phases [115]). One of the reasons of such an enhanced $n(T)$ in PbS is the high dislocation density $\delta \approx 10^{11}$ cm $^{-2}$. It has been shown that in the alkali-metals halides, the crystal electric field stability is disrupted on the atoms at the dislocation edges thus, generating charged interstitials and/or

vacancies [116]. Such a mechanism is relevant in the isostructural PbS, where both the interstitial Pb atoms and ionized S vacancies occur [57]. Also, dislocations have been shown to induce an n -type conductivity and enhanced charge carrier concentration in HgCdTe [117], Ge [118], Si [118,119], GaN thin films [120], etc.

The charge carrier mobility was further calculated from $\mu = (en\rho)^{-1}$. Its temperature dependence clearly reveals three regions (Fig. 8) corresponding to different scattering mechanisms [110,121]. So, for $T = 25$ – 100 K, the dependence $\mu \propto T^{-1/2}$ is observed, which indicates the domination of scattering by dislocations. This finding agrees well with high dislocation density $\delta \approx 10^{11}$ cm $^{-2} \gg 10^8$ cm $^{-2}$ (Fig. S1 in SM [62]) [110,121]. Further T increase results in the dominance of the charge carrier scattering on acoustic phonons, which is then reflected in the $\mu \propto T^{-3/2}$ dependence and is occurring in the ~ 100 – 170 K range. And finally, above ~ 170 K the charge carrier scattering occurs on both acoustic and optical phonons and thus, $\mu(T)$ becomes proportional to $\propto T^{-5/2}$. The switch to this third scattering mechanism is also visible as a kink at $T_k = 166$ K in $S(T)$. The $\mu \propto T^{-5/2}$ dependence is confirmed for synthetic PbS up to ~ 850 K [53].

The experimental effective mass of the charge carriers (m^*) normalized to the electron rest mass (m_e) has been calculated assuming energy independent scattering and parabolic-bands (corroborated by band structure calculations) with the formula

$$S(T) = \frac{8\pi^2 k_B^2}{3eh^2} \left(\frac{\pi}{3n}\right)^{2/3} m^* T \quad (6)$$

where k_B is the Boltzmann constant, h is the Planck constant, e is the elementary charge of an electron. The m^* were found to vary from 0.4 to 0.12 in the temperature range of 30–660 K, which is in fair agreement with the theoretically obtained values given in Table II.

E. Thermal transport and thermoelectric performance

The temperature dependence of the phononic thermal conductivity [$\kappa_{\text{ph}}(T)$] of natural PbS is shown in Fig. 9. Since galena was found to be a degenerate semiconductor (see discussion above) a deviation from the commonly used Lorenz number $L_0 = 2.44 \times 10^{-8}$ W Ω K $^{-2}$ is expected. Thus, its values were calculated from equation (7) [122],

$$L(T) = 1.5 + \exp\left(-\frac{|S(T)|}{116}\right) \quad (7)$$

where $|S(T)|$ is given in $\mu\text{V K}^{-1}$ and $L(T)$ in 10^{-8} W Ω K $^{-2}$. The obtained temperature dependence of the Lorenz number is presented in Fig. S3 in SM [62]. As expected, they strongly deviate from the average L_0 value at higher temperatures. Having $L(T)$, we further calculate the electronic thermal conductivity, given now as $\kappa_{\text{el}} = [L(T)/\rho(T)]T$. It is found to be negligibly small (i.e., less than $\sim 4\%$ of κ_{tot} , inset to Fig. S3 in SM [62]), thus indicating the phononic part ($\kappa_{\text{ph}} = \kappa_{\text{tot}} - \kappa_{\text{el}}$) to be the dominant one.

Interestingly, the phononic thermal conductivity approximately follows the Debye T^3 law (i.e., $\kappa_{\text{ph}} \propto T^3$) in the temperature range 2–5 K (fit is not shown in Fig. 9), which indicates the absence or minor contribution from point-inhomogeneities and -defects in the studied crystal. Materials

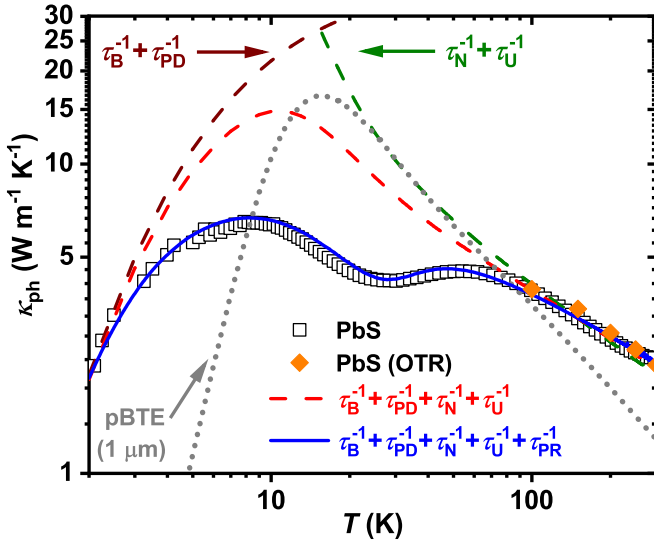


FIG. 9. Temperature dependencies of the phononic thermal conductivity κ_{ph} for the natural crystal of galena obtained from TTO measurements (black squares), by OTR method (orange diamonds), simulated from pBTE calculation (for a grain boundary size of 10 μm , gray dots), together with dominating low (brown dashed line) and high (green dashed line) temperature contributions. The thermal conductivity in absence of PR behavior is represented as the red dashed line.

revealing these scattering mechanisms are characterized by $\kappa_{\text{ph}} \propto T^{3-\alpha}$ dependencies [16,18], as it can be observed, for e.g., synthetic polycrystalline PbS [$\alpha \simeq 1.3(3) - 1.6(2)$] [54] and $\text{FeS}_{2-x}\text{As}_x$ [$\alpha \simeq 1.21(1) - 1.33(1)$] (point inhomogeneities were shown to play here the main role) [94] as well as for the FeS_2 natural crystal [$\alpha \simeq 0.095(4)$] (mainly due to point defects) [93].

Unexpectedly, further temperature increase led to the appearance of two maxima in PbS in both κ_{tot} and κ_{ph} : a sharp- (extending from 2 to 30 K and centered at $T_{\text{max}1} \approx 8$ K) and of a broad-one (extending from 30 to ~ 90 K and centered at $T_{\text{max}2} \approx 54$ K). The sharp maximum is nearly coinciding with those experimentally observed for natural single- [56] and synthetic bulk polycrystalline [54] samples as well as with the theoretically calculated ones in this paper (grey dots in Fig. 9) and reported in [89]. The appearance of a dip at $T_{\text{dip}} \approx 30$ K (i.e., between two maxima) in κ_{tot} and κ_{ph} is a hallmark of the so-called phonon resonance behavior, which has been observed in the ionic and isostructural to PbS mixed halides [25–27].

To shed light on the individual scattering mechanisms and the phonon resonance (PR) behavior in PbS, its κ_{ph} has been analyzed with the modified Debye-Callaway model [16],

$$\kappa_{\text{ph}} = \frac{k_{\text{B}}^4 T^3}{2\pi^2 v_{\text{S}} \hbar^3} \int_0^{\Theta_{\text{D}}/T} \frac{1}{\tau_{\text{tot}}^{-1}} \frac{x^4 e^x}{(e^x - 1)^2} dx \quad (8)$$

where $x = \hbar\omega/k_{\text{B}}T$, $v_{\text{S}} = 2110$ m s^{-1} is the average speed of sound [37,53] and τ_{tot}^{-1} is the total relaxation time. For classical cases (i.e., a single maximum in κ_{ph}), the latter is known to consist of the four main contributions,

$$\tau_{\text{tot}}^{-1} = \tau_{\text{B}}^{-1} + \tau_{\text{PD}}^{-1} + \tau_{\text{N}}^{-1} + \tau_{\text{U}}^{-1} \quad (9)$$

TABLE V. Constants (C_n) of the relaxation times obtained from Debye-Callaway model together with the respective formulas.

τ^{-1}	Equation [16]	C_n
τ_{B}^{-1}	v_{S}/C_1	$6.1(5) \times 10^{-5}$ m
τ_{PD}^{-1}	$C_2 x^4 T^4$	$1.6(1) \times 10^3$ s $^{-1}$ K $^{-4}$
τ_{N}^{-1}	$C_3 x^3 T^4$	$2.1(1) \times 10^3$ s $^{-1}$ K $^{-4}$
τ_{U}^{-1}	$C_4 x^2 T^2 e^{(-\Theta_{\text{D}}/3T)}$	$1.8(6) \times 10^7$ s $^{-1}$ K $^{-2}$

where τ_{B}^{-1} is staying for relaxation time of phonon scattering on grain boundaries, τ_{PD}^{-1} for point defects (these two effects dominate in the temperature range $T < 5$ K, brown dashed line in Fig. 9) whereas τ_{N}^{-1} and τ_{U}^{-1} indicate the normal and *umklapp* phonon processes, respectively (both dominate κ_{ph} for $T > 100$ K, green dashed line in Fig. 9). The fit to such an approach [e.g., Eqs. (8) and (9)] is shown by red dashed line in Fig. 9 and the obtained constants of the respective relaxation time are collected in Table V.

Since the classical model failed to describe the dip in κ_{ph} of PbS, the additional relaxation time τ_{PR}^{-1} staying for the PR behavior was introduced in the Eq. (9). τ_{PR}^{-1} [28] can be calculated from

$$\tau_{\text{PR}}^{-1} = \frac{C_5 \omega^2}{[(\omega_{\text{PR}}^2 - \omega^2)^2 + (C_6/\pi)^2 \omega^2 \omega_{\text{PR}}^2]}. \quad (10)$$

Now, including this τ_{PR}^{-1} in Eq. (8) and performing the fit the following constants $C_5 = 4.5(1) \times 10^{34}$ s $^{-3}$ and $C_6 = 2.9(1)$ together with characteristic PR frequency $\omega_{\text{PR}} = 3.8(1)$ THz were obtained (blue line in Fig. 9). The latter value fits to the frequencies region of 3–5.5 THz, where in PDR (Fig. 3) the sulfur optical modes with highest group velocities (Fig. S4 in SM [62]) contributing mainly to the lattice thermal conductivity are located. This coincidence is explaining the strong reduction of κ_{ph} (by $\approx 70\%$ in comparison with the classical Debye-Callaway model) in PbS (Fig. 9).

The here obtained $\omega_{\text{PR}} = 3.8(1)$ THz is by a factor of ≈ 3 –5 larger than those observed, for e.g., $\text{K}_{1-x}\text{Li}_x\text{Cl}$ [$\omega_{\text{PR}} = 1.2$ THz] and $\text{K}_{1-x}\text{Li}_x\text{Br}$ [$\omega_{\text{PR}} = 0.74$ THz], which could be due to different origins of PR in these materials. As it is known, phonon resonance behavior in halides was ascribed to impurity modes involving oscillations of the network hosting Li^+ -ions, which cannot be a case in the single-phase high quality PbS crystal studied here. Also, it cannot be due to “rattling” effect as it was observed in clathrates [24]. One possible scenario explaining PR in PbS would be a resonant scattering on the charged interstitials and/or vacancies arising from the enhanced dislocation density (larger by ≈ 4 orders of magnitude than those reported for synthetic crystals [56], see discussion above). However, this point would require some extensive theoretical studies, especially taking into account reports [123,124] where enhanced dislocation density was found to reduce κ_{ph} , however never triggered PR behavior.

The lattice thermal conductivity calculated from phonon Boltzmann transport equation (pBTE) assuming the scattering rates consisting of normal and *umklapp* three-phonon processes as well as grain boundary size to be of 1 μm is

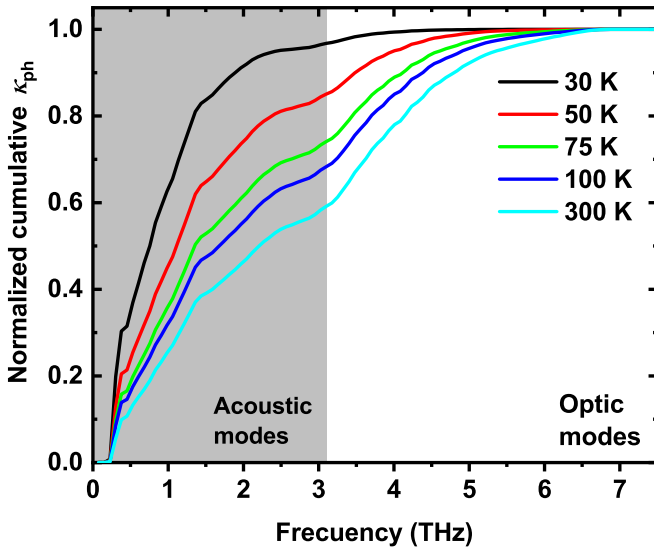


FIG. 10. Frequency-dependent normalized phononic thermal conductivity κ_{ph} for PbS calculated at diverse temperatures.

given in Fig. 9. It is deviating strongly from experimental data (see also inset to Fig. 11). This can be explained by few reasons, e.g., in the performed calculations were not included: (i) the scatterings due to point defects, dislocations, impurities, etc. and/or (ii) the strong temperature dependence of phonon branches (particularly TO modes) and four-phonon scatterings [125]. Hence, one can conclude, that the vibrational frequency shifts, together with strong higher-order anharmonic effects at finite temperatures [125], are one of the main reasons for the underestimation of κ_{ph} for $T > 100$ K in the performed calculations. In Fig. 10 the normalized cumulative thermal

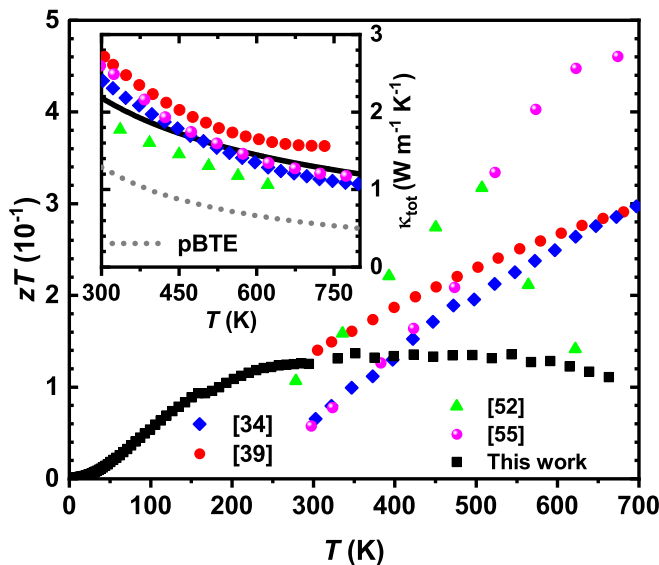


FIG. 11. Temperature-dependent thermoelectric figure-of-merit (zT) of natural PbS crystal (the values for $T > 300$ K were calculated using κ_{ph} obtained from the fit to the Debye-Callaway model) in comparison to synthetic counterparts. Inset: Total thermal conductivities (κ_{tot}) published for synthetic samples together with the theoretically calculated ones in this paper from the Debye-Callaway model (black line) and first principles pBTE.

conductivity for different temperatures are depicted. As it is clearly visible, the contributions to κ_{ph} from optical modes are increasing with temperature (e.g., it is only 5% at 30 K, reaches 29% at 75 K, and then achieves 45% at 300 K). Furthermore, the increase of the optical contribution to κ_{ph} is also related to the suppression of the acoustic modes with an increase in temperature [126] (see Fig. S4 in SM [62]).

The domination of *umklapp* three-phonon processes is frequently evidenced by $\kappa_{\text{ph}} \propto T^{-1}$ dependence for high temperatures. However, it is only seen for the theoretically simulated thermal conductivities for PbS (e.g., this paper and [89]). And indeed, the majority of the experimentally measured κ_{ph} [36,39,52,55] fit to $\kappa_1 + \kappa_0 T^{-1}$, confirming again the complexity of thermal transport in simple galena.

The temperature dependence of the thermoelectric (TE) figure-of-merit [$zT(T)$] for the natural crystal and undoped synthetic specimens are shown in Fig. 11. The reduced TE performance of the here studied PbS crystal is mainly due to enhanced electrical resistivity, compared to synthetic samples. The lower zT values are also confirming the purity of the natural crystal (as it is well known, the simple- or double doping of PbS, as well as its nanostructuring can improve its $zT(T)$ up to 1.23 at 923 K, as, e.g., reported for Cu- and Sb-doped galena [106]).

IV. CONCLUSIONS

Powder (PXRD) and single crystal x-ray diffraction performed on natural galena (PbS) crystal from Freiberg (Saxony, Germany) confirmed it to crystallize with the face-centred rock-salt (NaCl) structure. No additional peaks in PXRD together with energy dispersive x-ray spectroscopy analysis indicated that the mineral does not contain impurity phases. However, the Williamson-Hall plot revealed a tensile microstrain and an enhanced dislocation density $\delta \approx 10^{11} \text{ cm}^{-2}$. The low-temperature specific heat capacity is found to be mainly dominated by phononic contribution whereas magnetic susceptibility revealed the studied crystal to be a diamagnet. Both these findings confirm again the outstanding quality of the investigated specimen.

The theoretical DFT calculations and the evaluation of the energy dependence of absorption coefficient deduced from ellipsometric and IR spectroscopies indicated a direct energy gap of 0.23 eV and 0.4 eV, respectively for the studied PbS.

The five unexpectedly observed Raman active modes (i.e., forbidden by the factor group analysis) are obviously of second order. The analysis of their temperature dependencies let us to attribute the low frequency band to the Fröhlich resonance mechanism, whereas the explanation of the four high frequency ones is hampered due to the lack of a physical model that would describe second-order active Raman modes. The second-order origin of Raman active modes in PbS also did not allow us to separate the scattering of optical phonons into three-phonon and four-phonon decay mechanisms as it is normally a case if having the phononic part of thermal conductivity obtained by the optothermal Raman (OTR) technique.

As reported earlier for synthetic and natural galenas, we observe a metallic-like temperature dependence of electrical resistivity $\rho(T)$ for the here studied crystal (i.e., increasing

with T and of $\sim 10^{-4} \Omega \text{ m}$ order of magnitude). Such a behavior is mainly due to enhanced, as for a semiconductor, and temperature independent charge carrier concentration ($n \approx 10^{18} \text{ cm}^{-3}$). In our case it can be most probably explained by interstitial Pb atoms and/or ionized S vacancies generated along the dislocations edges in PbS. However, the studied specimen reveals for $T > 500 \text{ K}$ $\rho(T)$, which is by a factor of $\approx 2 - 3$ higher in comparison with those of synthetic galenas. This effect is attributed to the enhanced dislocation density. Interestingly, the temperature dependence of charge carrier mobility $\mu(T)$ confirms the domination of scattering on dislocations for $T < 100 \text{ K}$, which is reflected in $\mu \propto T^{-1/2}$ dependence. Further temperature increase resulted in the switch to $\mu \propto T^{-3/2}$ ($100 \text{ K} < T < 170 \text{ K}$) and to $\mu \propto T^{-5/2}$ ($170 \text{ K} < T < 300 \text{ K}$) dependencies, which confirm the scattering of charge carriers by acoustic- and by combined acoustic-optical-phonons, respectively. The former change of the type of scattering is also reflected by a kink at $T_k = 166 \text{ K}$ in the temperature evolution of the Seebeck coefficient $S(T)$.

The $S(T)$ dependence is mainly agreeing well with the simulated one. The only exception is observed for the low-temperature region (i.e., $T < 20 \text{ K}$), where instead of the expected linear increase it is described by a potential law: $S \propto T^{-7/2}$. Taking into account that such an effect occurs for $T < \theta_D/5 \approx 35 \text{ K}$, we ascribe it to a phonon-drag behavior. The energy gap $E_g^S = 0.51 \text{ eV}$ obtained from $S(T)$ by using the Goldsmid-Sharp formula is in a fair agreement with that determined from optical measurements. Furthermore, the effective masses of the charge carriers calculated from the temperature dependencies of Seebeck coefficient and carrier concentration are found to vary within $m^* \approx 0.4-0.12$, which is again in fair agreement with the values obtained from electronic band structure calculations.

The thermal conductivity of the natural PbS from Freiberg is dominated by phonons (i.e., κ_{ph}) and is unexpectedly revealing two maxima, which cannot be simulated by taking into account only normal and *umklapp* three-phonon scattering processes. Furthermore, the Debye-Callaway model, which additionally accounts for scattering of phonons by boundaries

and point defects could describe $\kappa_{\text{ph}}(T)$ in the temperature regions below $\sim 5 \text{ K}$ and above $\sim 100 \text{ K}$. The appearance of a minimum in $\kappa_{\text{ph}}(T)$ (i.e., a double maxima) in natural galena is a hallmark of the so-called phonon resonant behavior. Introducing the corresponding term into the classical Debye-Callaway model we were able to describe $\kappa_{\text{ph}}(T)$ in the whole temperature range obtaining a characteristic resonant frequency $\omega_{\text{PR}} = 3.8(1) \text{ THz}$. Since this value is in the same frequency region with the sulfur optical modes characterized by the highest group velocities (as shown by our simulations) and thus dominating the thermal transport in PbS, a remarkable (i.e., by $\sim 70\%$) damping of $\kappa_{\text{ph}}(T)$ is observed. The appearance of the phonon resonant behavior in natural PbS from Freiberg we ascribe to a possible resonant scattering on the charged interstitials and/or vacancies arising from the enhanced dislocation density.

In summary, the enhanced dislocation density is resulting in increase of the electrical resistivity and the absolute values of Seebeck coefficients as well as into reduction of the thermal conductivity of the studied here PbS crystal. Despite the latter two factors are beneficial for the thermoelectric performance, the former one is appeared to be the most crucial, which resulted in the lowering of the dimensionless figure-of-merit values at higher temperatures in comparison with the earlier studied synthetic samples.

ACKNOWLEDGMENTS

This work was performed within the Deutsche Forschungsgemeinschaft (DFG) Project No. 441856638. The DynaCool-12 system was acquired within the DFG Project No. 422219907. The authors thank U. Burkhardt, M. Eckert, S. Kostmann for metallographic preparation and analysis as well as G. Gärtner for performing IR optical measurements. We are grateful to T. Weigel and D.-C. Meyer for the assistance during single crystal diffraction experiments. The phonon transport calculations reported in this paper were partially performed at TUBITAK ULAKBIM, High Performance and Grid Computing Center (TRUBA resources).

-
- [1] International Energy Agency, World Energy Balances 2022, (2022).
 - [2] G. S. Nolas, J. Sharp, and J. Goldsmid, *Thermoelectrics: Basic Principles and New Materials Developments*, Vol. 45 (Springer Science & Business Media, New York, 2001).
 - [3] L. E. Bell, Cooling, heating, generating power, and recovering waste heat with thermoelectric systems, *Science* **321**, 1457 (2008).
 - [4] J. Sommerlatte, K. Nielsch, and H. Böttner, Thermoelektrische multitalente, *Phys. J.* **6**, 35 (2007).
 - [5] Q. Yan and M. G. Kanatzidis, High-performance thermoelectrics and challenges for practical devices, *Nat. Mater.* **21**, 503 (2022).
 - [6] J. He and T. M. Tritt, Advances in thermoelectric materials research: Looking back and moving forward, *Science* **357**, eaak9997 (2017).
 - [7] L.-D. Zhao, V. P. Dravid, and M. G. Kanatzidis, The panoramic approach to high performance thermoelectrics, *Energy Environ. Sci.* **7**, 251 (2014).
 - [8] M. Abramchuk, W. Schnelle, I. Veremchuk, A. Leithe-Jasper, Y. Grin, and R. Gumeniuk, Crystal structure, magnetic, electronic, and thermal transport properties of ternary compounds RRE₄ (RE = Ce, GdEr, Yb), *Eur. J. Inorg. Chem.* **2016**, 161 (2016).
 - [9] P. Wyzga, I. Veremchuk, C. Himcinschi, U. Burkhardt, W. Carrillo-Cabrera, M. Bobnar, C. Hennig, A. Leithe-Jasper, J. Kortus, and R. Gumeniuk, Indium thiospinel In_{1-x}□_xIn₂S₄ structural characterization and thermoelectric properties, *Dalton Trans.* **48**, 8350 (2019).
 - [10] P. Wyzga, W. Carrillo-Cabrera, L. Akselrud, I. Veremchuk, J. Wagler, C. Hennig, A. A. Tsirlin, A. Leithe-Jasper, E. Kroke, and R. Gumeniuk, Crystal structure, phase transition

- and properties of indium(III) sulfide, *Dalton Trans.* **49**, 15903 (2020).
- [11] P. Wyzga, I. Veremchuk, M. Bobnar, C. Hennig, A. Leithe-Jasper, and R. Gumeniuk, Ternary $M\text{In}_2\text{S}_4$ ($M = \text{Mn, Fe, Co, Ni}$) thiospinels crystal structure and thermoelectric properties, *Z. Anorg. Allg. Chem.* **646**, 1091 (2020).
- [12] P. Wyzga, I. Veremchuk, M. Bobnar, P. Koželj, S. Klenner, R. Pöttgen, A. Leithe-Jasper, and R. Gumeniuk, Structural peculiarities and thermoelectric study of iron indium thiospinel, *Chem. Eur. J.* **26**, 5245 (2020).
- [13] P. Wyzga, S. Grimm, V. Garbe, E. Zuñiga-Puelles, C. Himcinschi, I. Veremchuk, A. Leithe-Jasper, and R. Gumeniuk, Improving thermoelectric performance of indium thiospinel by Se- and Te-substitution, *J. Mater. Chem. C* **9**, 4008 (2021).
- [14] P. Wyzga, I. Veremchuk, P. Koželj, A. Leithe-Jasper, and R. Gumeniuk, Mn-for-Fe substitution in $\text{Fe}_{1-x}\text{Mn}_x\text{In}_2\text{S}_4$ thiospinel crystal structure and thermoelectric properties, *J. Phys. Chem. Solids* **152**, 109984 (2021).
- [15] S. Flipo, H. Rosner, M. Bobnar, K. O. Kvashnina, A. Leithe-Jasper, and R. Gumeniuk, Thermoelectricity and electronic properties of $\text{Y}_{1-x}\text{Ce}_x\text{CrB}_4$, *Phys. Rev. B* **103**, 195121 (2021).
- [16] T. M. Tritt, *Thermal Conductivity: Theory, Properties, and Applications* (Springer Science & Business Media, New York, 2005).
- [17] C. Chang and L.-D. Zhao, Anharmonicity and low thermal conductivity in thermoelectrics, *Mater. Today Phys.* **4**, 50 (2018).
- [18] E. S. Toberer, L. L. Baranowski, and C. Dames, Advances in thermal conductivity, *Annu. Rev. Mater. Res.* **42**, 179 (2012).
- [19] Y. Grin, Inhomogeneity and anisotropy of chemical bonding and thermoelectric properties of materials, *J. Solid State Chem.* **274**, 329 (2019).
- [20] S. Lee, K. Esfarjani, T. Luo, J. Zhou, Z. Tian, and G. Chen, Resonant bonding leads to low lattice thermal conductivity, *Nat. Commun.* **5**, 3525 (2014).
- [21] X. Qian, J. Zhou, and G. Chen, Phonon-engineered extreme thermal conductivity materials, *Nat. Mater.* **20**, 1188 (2021).
- [22] R. Gumeniuk, W. Schnelle, K. O. Kvashnina, and A. Leithe-Jasper, Kondo effect and thermoelectric transport in CePd_3Be_x , *J. Phys.: Condens. Matter* **28**, 165603 (2016).
- [23] R. Gumeniuk, Structural and physical properties of Remeika phases, in *Handbook on the Physics and Chemistry of Rare Earths* (Elsevier, Amsterdam, 2018), Vol. 54, pp. 43–143.
- [24] J. L. Cohn, G. S. Nolas, V. Fessatidis, T. H. Metcalf, and G. A. Slack, Glasslike Heat Conduction in High-Mobility Crystalline Semiconductors, *Phys. Rev. Lett.* **82**, 779 (1999).
- [25] F. C. Baumann, J. P. Harrison, R. O. Pohl, and W. D. Seward, Thermal conductivity in mixed alkali halides: $\text{KCl}:\text{Li}$ and $\text{KBr}:\text{Li}$, *Phys. Rev.* **159**, 691 (1967).
- [26] R. F. Caldwell and M. V. Klein, Experimental and theoretical study of phonon scattering from simple point defects in sodium chloride, *Phys. Rev.* **158**, 851 (1967).
- [27] J. P. Harrison, P. P. Peressini, and R. O. Pohl, Rotational degrees of freedom of molecules in solids. III. Thermal properties of $\text{RbCl}:\text{CN}$, *Phys. Rev.* **167**, 856 (1968).
- [28] R. O. Pohl, Thermal Conductivity and Phonon Resonance Scattering, *Phys. Rev. Lett.* **8**, 481 (1962).
- [29] R. Rounds, B. Sarkar, D. Alden, Q. Guo, A. Klump, C. Hartmann, T. Nagashima, R. Kirste, A. Franke, M. Bickermann, Y. Kumagai, Z. Sitar, and R. Collazo, The influence of point defects on the thermal conductivity of AlN crystals, *J. Appl. Phys.* **123**, 185107 (2018).
- [30] H. Liu, J. Yang, X. Shi, S. A. Danilkin, D. Yu, C. Wang, W. Zhang, and L. Chen, Reduction of thermal conductivity by low energy multi-Einstein optic modes, *J. Materiomics* **2**, 187 (2016).
- [31] M. Lach-hab, D. A. Papaconstantopoulos, and M. J. Mehl, Electronic structure calculations of lead chalcogenides PbS, PbSe, PbTe, *J. Phys. Chem. Solids* **63**, 833 (2002).
- [32] J. Yang, X. Zhang, G. Liu, L. Zhao, J. Liu, Z. Shi, J. Ding, and G. Qiao, Multiscale structure and band configuration tuning to achieve high thermoelectric properties in n-type PbS bulks, *Nano Energy* **74**, 104826 (2020).
- [33] Y. Xiao, D. Wang, Y. Zhang, C. Chen, S. Zhang, K. Wang, G. Wang, S. J. Pennycook, G. J. Snyder, H. Wu *et al.*, Band sharpening and band alignment enable high quality factor to enhance thermoelectric performance in n-type PbS, *J. Am. Chem. Soc.* **142**, 4051 (2020).
- [34] L.-D. Zhao, J. He, S. Hao, C.-I. Wu, T. P. Hogan, C. Wolverton, V. P. Dravid, and M. G. Kanatzidis, Raising the thermoelectric performance of p-type PbS with endotaxial nanostructuring and valence-band offset engineering using CdS and ZnS, *J. Am. Chem. Soc.* **134**, 16327 (2012).
- [35] Y. Zhang, X. Ke, C. Chen, J. Yang, and P. R. C. Kent, Thermodynamic properties of PbTe, PbSe, and PbS: First-principles study, *Phys. Rev. B* **80**, 024304 (2009).
- [36] L.-D. Zhao, J. He, C.-I. Wu, T. P. Hogan, X. Zhou, C. Uher, V. P. Dravid, and M. G. Kanatzidis, Thermoelectrics with earth abundant elements: High performance p-type PbS nanostructured with SrS and CaS, *J. Am. Chem. Soc.* **134**, 7902 (2012).
- [37] J. M. Skelton, S. C. Parker, A. Togo, I. Tanaka, and A. Walsh, Thermal physics of the lead chalcogenides PbS, PbSe, and PbTe from first principles, *Phys. Rev. B* **89**, 205203 (2014).
- [38] G. U. von Oertzen, R. Jones, and A. Gerson, Electronic and optical properties of Fe, Zn and Pb sulfides, *Phys. Chem. Miner.* **32**, 255 (2005).
- [39] Y.-L. Pei and Y. Liu, Electrical and thermal transport properties of Pb-based chalcogenides: PbTe, PbSe, and PbS, *J. Alloys Compd.* **514**, 40 (2012).
- [40] S. Johnsen, J. He, J. Androulakis, V. P. Dravid, I. Todorov, D. Y. Chung, and M. G. Kanatzidis, Nanostructures boost the thermoelectric performance of PbS, *J. Am. Chem. Soc.* **133**, 3460 (2011).
- [41] H. Kanazawa and S. Adachi, Optical properties of PbS, *J. Appl. Phys.* **83**, 5997 (1998).
- [42] J. W. Anthony, R. A. Bideaux, K. Bladh, and M. C. Nichols, *Handbook of Mineralogy: Volume I. Elements, Sulfides, Sulfosalts* (Mineral Data Publishing, Tucson, AZ, 1990).
- [43] C. S. Hurlbut, E. S. Dana, and W. E. Sharp, *Dana's Minerals and How to Study Them (After Edward Salisbury Dana)* (John Wiley & Sons, Hoboken, NJ, 1998).
- [44] L. S. Ramsdell, The crystal structure of some metallic sulfides, *Am. Mineral.* **10**, 281 (1925).
- [45] T. H. Lee, The (pre-) history of the integrated circuit: a random walk, *IEEE Solid-State Circ. Soc. Newsletter* **12**, 16 (2007).
- [46] H. Liu and L. Chang, Phase relations in the system PbS-PbSe-PbTe, *Mineral. Mag.* **58**, 567 (1994).
- [47] R. G. Coleman, The natural occurrence of galena-clausthalite solid solution series, *Am. Mineral.* **44**, 166 (1959).

- [48] D. Khokhlov, *Lead Chalcogenides: Physics and Applications* (CRC Press, Boca Raton, FL, 2002).
- [49] I. I. Ravich, *Semiconducting Lead Chalcogenides*, Vol. 5 (Springer Science & Business Media, New York, 2013).
- [50] Y. Shi, C. Sturm, and H. Kleinke, Chalcogenides as thermoelectric materials, *J. Solid State Chem.* **270**, 273 (2019).
- [51] A. P. Gonçalves and C. Godart, New promising bulk thermoelectrics: intermetallics, pnictides and chalcogenides, *Eur. Phys. J. B* **87**, 1 (2014).
- [52] H. Zhang, H. Wang, H. Zhu, H. Li, T. Su, S. Li, M. Hu, and H. Fan, Hydrothermal synthesis and thermoelectric properties of PbS, *Mater. Sci.-Pol.* **34**, 754 (2016).
- [53] H. Wang, E. Schechtel, Y. Pei, and G. J. Snyder, High thermoelectric efficiency of n-type PbS, *Adv. Energy Mater.* **3**, 488 (2013).
- [54] C. M. Zeuthen, P. S. Thorup, N. Roth, and B. B. Iversen, Reconciling crystallographic and physical property measurements on thermoelectric lead sulfide, *J. Am. Chem. Soc.* **141**, 8146 (2019).
- [55] L. Zhao, J. Yang, B. Lu, X. Zhang, J. Hu, W. Xie, H. Shao, G. Liu, S. Hussain, Z. Shi *et al.*, Enhanced thermoelectric properties of n-type Cl doped PbS-based materials via Bi alloying, *J. Alloys Compd.* **859**, 157788 (2021).
- [56] D. Greig, Thermoelectricity and thermal conductivity in the lead sulfide group of semiconductors, *Phys. Rev.* **120**, 358 (1960).
- [57] L. S. Milevskii, T. M. Tkacheva, A. A. Urusovskaya, and G. G. Knab, Connection between electrical and deformation characteristics of PbS crystals, *Krist. Techn.* **16**, 95 (1981).
- [58] B. K. Agrawal and G. Verma, Lattice thermal conductivity of ZnF₂, CaF₂, PbS and InSb at low temperatures, *Physica* **28**, 599 (1962).
- [59] T. Seifert and D. Sandmann, Mineralogy and geochemistry of indium-bearing polymetallic vein-type deposits: Implications for host minerals from the Freiberg district, Eastern Erzgebirge, Germany, *Ore Geo. Rev.* **28**, 1 (2006).
- [60] CrysAlisPRO, Oxford Diffraction /Agilent Technologies UK Ltd, Yarnton, England.
- [61] L. Akselrud and Y. Grin, WinCSD: Software package for crystallographic calculations (version 4), *J. Appl. Cryst.* **47**, 803 (2014).
- [62] See Supplemental Material at <http://link.aps.org/supplemental/10.1103/PhysRevB.107.195203> for results of Williamson-Hall plot, temperature dependencies of Raman peak positions, Lorenz numbers and electrical contribution to the thermal conductivity as well as detailed analysis of phonon density of states.
- [63] E. Zuñiga-Puelles, R. Cardoso-Gil, A. Özden, N. Bulut, V. Svitlyk, C. Himcinschi, J. Kortus, and R. Gumeniuk, Low thermal conductivity in bournonite PbCuSbS₃: A comprehensive study, *Phys. Rev. B* **106**, 195201 (2022).
- [64] A. Özden, E. Zuñiga-Puelles, J. Kortus, R. Gumeniuk, and C. Himcinschi, Thermal conductivity and phonon anharmonicity of chemical vapor transport grown and mineral FeS₂ single crystals: An optothermal Raman study, *J. Raman Spectrosc.* **54**, 84 (2023).
- [65] K. Koepf and H. Eschrig, Full-potential nonorthogonal local-orbital minimum-basis band-structure scheme, *Phys. Rev. B* **59**, 1743 (1999).
- [66] J. P. Perdew and Y. Wang, Accurate and simple analytic representation of the electron-gas correlation energy, *Phys. Rev. B* **45**, 13244 (1992).
- [67] P. Giannozzi Jr, O. Andreussi, T. Brumme, O. Bunau, M. B. Nardelli, M. Calandra, R. Car, C. Cavazzoni, D. Ceresoli, M. Cococcioni *et al.*, Advanced capabilities for materials modelling with quantum espresso, *J. Phys.: Condens. Matter* **29**, 465901 (2017).
- [68] G. K. Madsen and D. J. Singh, Boltztrap: a code for calculating band-structure dependent quantities, *Comput. Phys. Commun.* **175**, 67 (2006).
- [69] J. P. Perdew, K. Burke, and M. Ernzerhof, Generalized Gradient Approximation Made Simple [Phys. Rev. Lett. 77, 3865 (1996)], *Phys. Rev. Lett.* **78**, 1396(E) (1997).
- [70] A. Dal Corso, Pseudopotentials periodic table: From H to Pu, *Comput. Mater. Sci.* **95**, 337 (2014).
- [71] G. Kresse and J. Furthmüller, Efficient iterative schemes for *ab initio* total-energy calculations using a plane-wave basis set, *Phys. Rev. B* **54**, 11169 (1996).
- [72] G. Kresse and D. Joubert, From ultrasoft pseudopotentials to the projector augmented-wave method, *Phys. Rev. B* **59**, 1758 (1999).
- [73] A. Togo and I. Tanaka, First principles phonon calculations in materials science, *Scr. Mater.* **108**, 1 (2015).
- [74] S. Baroni, S. de Gironcoli, A. Dal Corso, and P. Giannozzi, Phonons and related crystal properties from density-functional perturbation theory, *Rev. Mod. Phys.* **73**, 515 (2001).
- [75] W. Li, J. Carrete, N. A. Katcho, and N. Mingo, Shengbte: A solver of the Boltzmann transport equation for phonons, *Comput. Phys. Commun.* **185**, 1747 (2014).
- [76] J. C. Guiming Guo, Xiaolong Yang and W. Li, Revisiting the thermal conductivity of Si, Ge and diamond from first principles: Roles of atomic mass and interatomic potential, *J. Phys.: Condens. Matter* **33**, 285702 (2021).
- [77] Y. Noda, K. Masumoto, S. Ohba, Y. Saito, K. Toriumi, Y. Iwata, and I. Shibuya, Temperature dependence of atomic thermal parameters of lead chalcogenides, PbS, PbSe and PbTe, *Acta Cryst. C* **43**, 1443 (1987).
- [78] J. Emsley, *The Elements* (Oxford University Press, Oxford, 1998).
- [79] B. Himabindu, N. Latha Devi, and B. Rajini Kanth, Microstructural parameters from x-ray peak profile analysis by Williamson-Hall models; A review, *Mater. Today* **47**, 4891 (2021).
- [80] M. Dongol, A. El-Denglawey, A. Elhady, and A. Abuelwafa, Structural properties of nano 5, 10, 15, 20-tetraphenyl-21H,23H-porphine nickel (II) thin films, *Curr. Appl. Phys.* **12**, 1334 (2012).
- [81] M. Dongol, A. El-Denglawey, M. Abd El Sadek, and I. Yahia, Thermal annealing effect on the structural and the optical properties of nano CdTe films, *Optik* **126**, 1352 (2015).
- [82] M. Elcombe, The crystal dynamics of lead sulphide, *Proc. R. Soc. London A* **300**, 210 (1967).
- [83] H. Alperin, S. Pickart, J. Rhyne, and V. Minkiewicz, Softening of the transverse-optic mode in PbTe, *Phys. Lett. A* **40**, 295 (1972).
- [84] W. J. Daughton, C. W. Tompson, and E. Gurmen, Lattice instability and phonon lifetimes in Pb_{1-x}Sn_xTe alloys, *J. Phys. C: Solid State Phys.* **11**, 1573 (1978).

- [85] C. W. Li, O. Hellman, J. Ma, A. F. May, H. B. Cao, X. Chen, A. D. Christianson, G. Ehlers, D. J. Singh, B. C. Sales, and O. Delaire, Phonon Self-Energy and Origin of Anomalous Neutron Scattering Spectra in SnTe and PbTe Thermoelectrics, *Phys. Rev. Lett.* **112**, 175501 (2014).
- [86] G. D. Smith, S. Firth, R. J. H. Clark, and M. Cardona, First- and second-order Raman spectra of galena (PbS), *J. Appl. Phys.* **92**, 4375 (2002).
- [87] R. Sherwin, R. J. Clark, R. Lauck, and M. Cardona, Effect of isotope substitution and doping on the Raman spectrum of galena (PbS), *Solid State Commun.* **134**, 565 (2005).
- [88] K. S. Knight, Low temperature thermoelastic properties of galena in a simple, self-consistent, two-term Debye model, *Phys. Chem. Miner.* **42**, 235 (2015).
- [89] L. Wei, J.-F. Chen, Q.-Y. He, and W. Teng, Study of lattice thermal conductivity of PbS, *J. Alloys Compd.* **584**, 381 (2014).
- [90] G. A. Bain and J. F. Berry, Diamagnetic corrections and Pascal's constants, *J. Chem. Educ.* **85**, 532 (2008).
- [91] M. Feig, W. Schnelle, A. Maisuradze, A. Amon, C. Baines, M. Nicklas, S. Seiro, L. Howald, R. Khasanov, A. Leithe-Jasper, and R. Gumeniuk, Conventional isotropic *s*-wave superconductivity with strong electron-phonon coupling in $\text{Sc}_5\text{Rh}_6\text{Sn}_{18}$, *Phys. Rev. B* **102**, 024508 (2020).
- [92] T. Hesjedal, U. Kretzer, and A. Ney, Magnetic susceptibility of *n*-type GaAs, *Semicond. Sci. Technol.* **27**, 055018 (2012).
- [93] E. Zuñiga-Puelles, R. Cardoso-Gil, M. Bobnar, I. Veremchuk, C. Himcinschi, C. Hennig, J. Kortus, G. Heide, and R. Gumeniuk, Structural stability and thermoelectric performance of high quality synthetic and natural pyrites (FeS_2), *Dalton Trans.* **48**, 10703 (2019).
- [94] E. Zuñiga-Puelles, R. Cardoso-Gil, M. Bobnar, I. Veremchuk, G. Heide, and R. Gumeniuk, Electrical and thermal transport properties of natural and synthetic $\text{FeAs}_x\text{S}_{2-x}$ ($x \leq 0.01$), *J. Phys. Chem. Solids* **150**, 109809 (2021).
- [95] K. A. Borup, J. De Boor, H. Wang, F. Drymiotis, F. Gascoin, X. Shi, L. Chen, M. I. Fedorov, E. Müller, B. B. Iversen *et al.*, Measuring thermoelectric transport properties of materials, *Eng. Env. Sci.* **8**, 423 (2015).
- [96] E. D. Palik, *Handbook of Optical Constants of Solids*, Vol. 3 (Academic Press, New York, 1998).
- [97] K.-H. Hellwege, Elastic, piezoelectric, pyroelectric, piezooptic, electrooptic constants, and nonlinear dielectric susceptibilities of crystal, in *Landolt Bornstein, Numerical Data and Functional Relationship in Science and Technology* (Springer-Verlag, Berlin, 1979).
- [98] E. Burstein, F. A. Johnson, and R. Loudon, Selection rules for second-order infrared and Raman processes in the rocksalt structure and interpretation of the Raman spectra of NaCl, KBr, and NaI, *Phys. Rev.* **139**, A1239 (1965).
- [99] M. Born and M. Bradburn, The theory of the Raman effect in crystals, in particular rock-salt, *Proc. R. Soc. London A* **188**, 161 (1947).
- [100] P. G. Etchegoin, M. Cardona, R. Lauck, R. Clark, J. Serrano, and A. Romero, Temperature-dependent Raman scattering of natural and isotopically substituted PbS, *Phys. Status Solidi B* **245**, 1125 (2008).
- [101] S. V. Ovsyannikov, V. V. Shchennikov, Y. S. Ponosov, S. V. Gudina, V. G. Guk, E. P. Skipetrov, and V. E. Mogilenskikh, Application of the high-pressure thermoelectric technique for characterization of semiconductor microsamples: PbX-based compounds, *J. Phys. D: Appl. Phys.* **37**, 1151 (2004).
- [102] M. Balkanski, R. F. Wallis, and E. Haro, Anharmonic effects in light scattering due to optical phonons in silicon, *Phys. Rev. B* **28**, 1928 (1983).
- [103] M. V. Abrashev, A. P. Litvinchuk, C. Thomsen, and V. N. Popov, Fröhlich-interaction-induced multiphonon Raman scattering in SrCuO_2 and $\text{Sr}_{0.5}\text{Ca}_{0.5}\text{CuO}_2$, *Phys. Rev. B* **55**, R8638 (1997).
- [104] Z. Zhao, J. Elwood, and M. A. Carpenter, Phonon anharmonicity of PdO studied by Raman spectrometry, *J. Phys. Chem. C* **119**, 23094 (2015).
- [105] S. S. Majid, D. K. Shukla, F. Rahman, S. Khan, K. Gautam, A. Ahad, S. Francoual, R. J. Choudhary, V. G. Sathe, and J. Strempler, Insulator-metal transitions in the *T* phase Cr-doped and *M1* phase undoped VO_2 thin films, *Phys. Rev. B* **98**, 075152 (2018).
- [106] M. Zhao, C. Chang, Y. Xiao, R. Gu, J. He, and L.-D. Zhao, Investigations on distinct thermoelectric transport behaviors of Cu in *n*-type PbS, *J. Alloys Compd.* **781**, 820 (2019).
- [107] R. Gross, A. Marx, D. Einzel, and S. Geprägs, *Festkörperphysik: Aufgaben und Lösungen* (De Gruyter, New York, 2018).
- [108] H. Goldsmid and J. Sharp, Estimation of the thermal band gap of a semiconductor from Seebeck measurements, *J. Electron. Mater.* **28**, 869 (1999).
- [109] Z. M. Gibbs, H.-S. Kim, H. Wang, and G. J. Snyder, Band gap estimation from temperature dependent Seebeck measurement-Deviations from the $2e|S|_{\text{max}}T_{\text{max}}$ relation, *Appl. Phys. Lett.* **106**, 022112 (2015).
- [110] C. Herring, Theory of the thermoelectric power of semiconductors, *Phys. Rev.* **96**, 1163 (1954).
- [111] A. T. Duong, V. Q. Nguyen, G. Duvjir, V. T. Duong, S. Kwon, J. Y. Song, J. K. Lee, J. E. Lee, S. Park, T. Min *et al.*, Achieving $ZT = 2.2$ with Bi-doped *n*-type SnSe single crystals, *Nat. Commun.* **7**, 13713 (2016).
- [112] K. Zhao, A. B. Blichfeld, E. Eikeland, P. Qiu, D. Ren, B. B. Iversen, X. Shi, and L. Chen, Extremely low thermal conductivity and high thermoelectric performance in liquid-like $\text{Cu}_2\text{Se}_{1-x}\text{S}_x$ polymorphic materials, *J. Mater. Chem. A* **5**, 18148 (2017).
- [113] Y. Wang, X. Zhang, Y. Wang, H. Liu, and J. Zhang, Enhanced thermoelectric properties of *n*-type Mg_3Sb_2 by excess magnesium and tellurium doping, *Phys. Status Solidi A* **216**, 1800811 (2019).
- [114] X. Chen, H. Wu, J. Cui, Y. Xiao, Y. Zhang, J. He, Y. Chen, J. Cao, W. Cai, S. J. Pennycook *et al.*, Extraordinary thermoelectric performance in *n*-type manganese doped Mg_3Sb_2 Zintl: High band degeneracy, tuned carrier scattering mechanism and hierarchical microstructure, *Nano Energy* **52**, 246 (2018).
- [115] M. Wolf, R. Hinterding, and A. Feldhoff, High power factor vs. high zT – A review of thermoelectric materials for high-temperature application, *Entropy* **21**, 1058 (2019).

- [116] N. A. Tyapunina and E. P. Belozeroва, Charged dislocations and properties of alkali halide crystals, *Sov. Phys. Usp.* **31**, 1060 (1988).
- [117] J. Tregilgas, T. Polgreen, and M. Chen, Dislocations and electrical characteristics of HgCdTe, *J. Cryst. Growth* **86**, 460 (1988).
- [118] W. Schröter and H. Cerva, Interaction of point defects with dislocations in silicon and germanium: Electrical and optical effects, *Solid State Phenom.* **85–86**, 67 (2002).
- [119] P. Omling, E. R. Weber, L. Montelius, H. Alexander, and J. Michel, Electrical properties of dislocations and point defects in plastically deformed silicon, *Phys. Rev. B* **32**, 6571 (1985).
- [120] H. M. Ng, D. Doppalapudi, T. D. Moustakas, N. G. Weimann, and L. F. Eastman, The role of dislocation scattering in n-type GaN films, *Appl. Phys. Lett.* **73**, 821 (1998).
- [121] S. S. Li, *Semiconductor Physical Electronics* (Springer, New York, 2006).
- [122] H.-S. Kim, Z. M. Gibbs, Y. Tang, H. Wang, and G. J. Snyder, Characterization of Lorenz number with Seebeck coefficient measurement, *APL Mater.* **3**, 041506 (2015).
- [123] M. Johanning, L. Porz, J. Dong, A. Nakamura, J.-F. Li, and J. Rödel, Influence of dislocations on thermal conductivity of strontium titanate, *Appl. Phys. Lett.* **117**, 021902 (2020).
- [124] B. Sun, G. Haunschild, C. Polanco, J. Ju, L. Lindsay, G. Koblmüller, and Y. K. Koh, Dislocation-induced thermal transport anisotropy in single-crystal group-III nitride films, *Nat. Mater.* **18**, 136 (2019).
- [125] Y. Xia, Revisiting lattice thermal transport in PbTe: The crucial role of quartic anharmonicity, *Appl. Phys. Lett.* **113**, 073901 (2018).
- [126] O. Delaire, J. Ma, K. Marty, A. F. May, M. A. McGuire, M.-H. Du, D. J. Singh, A. Podlesnyak, G. Ehlers, M. Lumsden *et al.*, Giant anharmonic phonon scattering in PbTe, *Nat. Mater.* **10**, 614 (2011).